

Rapid Construction of 3D Biomimetic Capillary Networks with Complex Morphology Using Dynamic Holographic Processing

Bowen Song, Chaowei Wang, Shengying Fan, Leran Zhang, Chenchu Zhang, Wei Xiong, Yanlei Hu, Jiaru Chu, Dong Wu, and Jiawen Li*

Microvascular networks (MVNs) are crucial transportation systems in living creatures for nutrient distribution, fluid flow, energy transportation and so on. However, artificial manufacturing of MVNs, especially capillary networks with diameters (average $6 \approx 9 \mu\text{m}$), has always been a problem and bottleneck in tissue engineering due to the lack of efficient manufacturing methods. Herein, a dynamic holographic processing method is reported for producing 3D capillary networks with complex biomimetic morphologies. Combining the axial scanning of the focused beam and the dynamic display of holograms, biomimetic bifurcated microtubes, and porous microtubes with programmable morphologies are rapidly produced by two-photon polymerization (TPP). As a proof-of-concept demonstration, porous microtubes are used as 3D capillary network scaffolds for culturing human umbilical vein endothelial cells (HUVECs) to facilitate the exchange of nutrients and metabolites. Endothelial cells around the vascular scaffolds manifest obvious tight connections and 3D coverage after 3 days in vitro, which reveals that the scaffolds play a significant role in the morphology of dense vascularization. This flexible and rapid method of producing capillary networks provides a versatile platform for vascular physiology, tissue regeneration, and other biomedical areas.

component of tissue, providing nutrients to organs and transporting oxygen and metabolic waste.^[5,6] Due to the lack of a suitable blood supply system for tissues constructed in vitro, only skin,^[7] cartilage,^[8] and bone tissue engineering,^[9] products have been successfully applied in clinical practice. Artificial hearts,^[10–12] livers,^[13–15] lungs,^[16–18] and other organs have been printed successfully in recent years, but artificial manufacturing of MVNs has always been a challenge and bottleneck in tissue engineering. MVNs, especially capillary networks with diameters (average $6 \approx 9 \mu\text{m}$) connected through complex branches, are difficult to obtain due to the lack of efficient manufacturing methods.^[19,20]

To solve the problem of nutrient and waste transportation in tissues, microfluidic chip processing technology was used to construct MVNs.^[21–23] However, the cross-section of the manufactured channels is rectangular and the vast majority of channels are distributed on a two-dimensional plane, making it difficult to form an ideal 3D microchannel. In addition, researchers

have induced the formation of new blood vessels in the inner wall of blood vessels through angiogenesis.^[24–26] Using growth factors to induce endothelial cell proliferation can form new blood vessels, however, this method cannot accurately control the growth and infiltration of microvessels, and the uncontrolled and

1. Introduction

The purpose of tissue engineering is to construct tissues and organs with physiological functions for repairing diseases and defects in the human body.^[1–4] Blood vessels are an important

B. Song, C. Wang, L. Zhang, Y. Hu, J. Chu, D. Wu, J. Li
CAS Key Laboratory of Mechanical Behavior and Design of Materials
Department of Precision Machinery and Precision Instrumentation
University of Science and Technology of China
Hefei 230027, China
E-mail: jwl@ustc.edu.cn

S. Fan
Laser Institute
Qilu University of Technology (Shandong Academy of Sciences)
Jinan 250104, China

C. Zhang
Anhui Province Key Lab of Aerospace Structural Parts Forming
Technology and Equipment
Institute of Industry & Equipment Technology
Hefei University of Technology
Hefei 230009, China

W. Xiong
Wuhan National Laboratory for Optoelectronics and School of Optical
and Electronic Information
Huazhong University of Science and Technology
Wuhan 430074, China

 The ORCID identification number(s) for the author(s) of this article can be found under <https://doi.org/10.1002/adfm.202305245>

DOI: 10.1002/adfm.202305245

harmful growth of new blood vessels may cause tissue lesions. As an alternative method mentioned above, the molding method has gradually received attention in recent years. They have been adopted to fabricate carbohydrate glass,^[27] or bioink,^[28] into biomimetic microvascular network scaffolds with different morphologies. The cell-loaded hydrogel was poured on the scaffolds, and then the scaffold material was dissolved with water to form microvascular networks with a diameter of $50 \approx 750 \mu\text{m}$. Then, endothelial cell growth was carried out to mimic blood vessel functionalities in the human body. However, all these methods can hardly obtain 3D microvascular networks with different morphologies and microtube diameters of $\approx 10 \mu\text{m}$, which approaches the scale of real capillary blood vessels. Therefore, a method with high resolution and 3D processing ability to construct capillary networks with complex morphologies is urgently needed.

Femtosecond direct laser writing (FsDLW) by two-photon polymerization (TPP) shows sufficient flexibility in producing complex 3D microstructures with high resolution.^[29–32] There have been some 3D microstructures realized by TPP used as 3D microvascular network scaffolds for studying cell behaviors.^[33,34] However, the point-by-point scanning strategy limits the efficiency of traditional FsDLW processing. Combined with spatial light modulation technology, the modulated laser beam can be used to promote the TPP efficiency and complex 3D structures can be fabricated rapidly and flexibly.^[35–38] The Bessel beam, which has an annular intensity distribution, is particularly suitable for processing microtubes with tunable diameters and variable annular cross sections.^[39,40] However, capillary networks in vivo are a complex and asymmetric structures with bifurcated morphologies. To the best of our knowledge, biomimetic capillary network scaffolds with micron diameters have not been fabricated by spatial light modulated femtosecond laser TPP technology to study cellular behaviors.

In this work, we propose a dynamic holographic processing method to rapidly fabricate bifurcated microtube networks with complex morphologies and porous microtubes with controllable parameters (pore size, number, and location). Based on local grayscale phase modulation, the Bessel beam was tailored to different gap-ring beams. The influence of tuning the center angle θ of computer-generated holograms (CGHs) on the center angle of gap-ring structures is discussed in detail. On this basis, porous microtubes are used as scaffolds for culturing human umbilical vein endothelial cells (HUVECs), which facilitates the exchange of substances. Endothelial cells around the vascular scaffolds have obvious tight connections and 3D coverage after 3 days, which reveals that the scaffolds play a significant role in the morphology of dense vascularization. This rapid processing method may represent a promising tool for producing biomimetic capillary networks and has broad applications in biomedical fields such as drug screening, 3D cell cultures and vascular physiology.

2. Results

2.1. Generation and Quantitative Control of Gap-Ring Beam for Fabricating Microstructure

The main concept diagram of the programmable fabrication of biomimetic capillary network scaffolds in our experiment is il-

lustrated in **Figure 1a**. The femtosecond laser beam is modulated into a gap-ring Bessel beam by predesigned computer-generated holograms (CGHs) loaded on the spacial light modulator (SLM). The gap-ring Bessel beam CGH is composed of four parts: spiral phase plate (SPP), axicon, blazed grating (BG) and local grayscale phase (LGP) (Figure 1b). The SPP provides an azimuthal phase distribution of $n\varphi$, and its topological charge n is an integer and represents the order of the Bessel beam. The axicon has a radial phase distribution of $2\pi r/r_0$, and r_0 is the radius of the axicon. BG provides a $2\pi y/\Delta$ phase distribution and is added to separate the diffractive lights of different orders, where Δ represents the period of the blazed grating. The function of the local grayscale phase is to adjust the intensity distribution of the Bessel beam to generate an asymmetric gap-ring beam.

The phase distribution of the Bessel beam in the Cartesian coordinate system is presented as:

$$Ph_{\text{Bessel}}(x, y) = \text{mod} \left(n\varphi + \frac{2\pi r}{r_0} + \frac{2\pi y}{\Delta}, 2\pi \right) \quad (1)$$

where $\varphi = \arctan(y/x)$ is the polar angle and $r = \sqrt{x^2 + y^2}$ is the polar radius. By changing the topological charge n and axicon radius r_0 , microtubes with adjustable diameters ($6 \approx 16 \mu\text{m}$) (Figure S1, Supporting Information) can be flexibly manufactured. This size is very close to the diameter of real capillaries and is very suitable for simulating capillary scaffolds.

The LGP can be divided into two zones: the white zone represents the unmodulated region with an unchanged $Ph_{\text{Bessel}}(x, y)$, while the black zone indicates that $Ph_{\text{Bessel}}(x, y)$ is modulated to zero. Therefore, the phase distribution of the gap-ring Bessel CGH is presented as:

$$Ph_{\text{Gap-ring Bessel}} = \begin{cases} 0 & \varphi \in \theta \\ Ph_{\text{Bessel}}(x, y) & \text{else} \end{cases} \quad (2)$$

where the modulation area $\theta = [\varphi_1, \varphi_2]$, φ_1 , and φ_2 represent the clockwise and counterclockwise angles from the x -axis to the edge of the fan-shaped area, respectively. (Figure S2, supporting information).

After being reflected by the SLM, the modulated gap-ring Bessel beam is focused into the photoresist (SZ 2080) by an oil-immersion objective lens ($60\times$, $NA = 1.35$). Simulated and experimental light fields modulated by different CGHs are illustrated in Figure 1c to show the principle of the local grayscale phase modulation and the controllable energy distribution of the gap-ring Bessel beam. All the CGHs have the same $n = 40$ and $r_0 = 400$ but different θ , 270° , 210° , 150° , 90° , 50° , and 10° , respectively. The scanning electron microscopy (SEM) images of gap-ring structures have good consistency with the corresponding simulated light intensity distributions. The single exposure time and laser power used were 1000 ms and 110 mW, respectively. Since TPP is a nonlinear polymerization process, the laser power has a great impact on the morphology of the structure. Higher laser power will cause a stronger photopolymerization reaction, resulting in a smaller center angle α_2 . To study the influence of laser power on gap-ring structures, three groups of different laser powers (160, 180, and 200 mW) were used to process the same CGHs (Figure 1d; Figure S3, Supporting Information). The curves shifted to the left with increasing laser power.

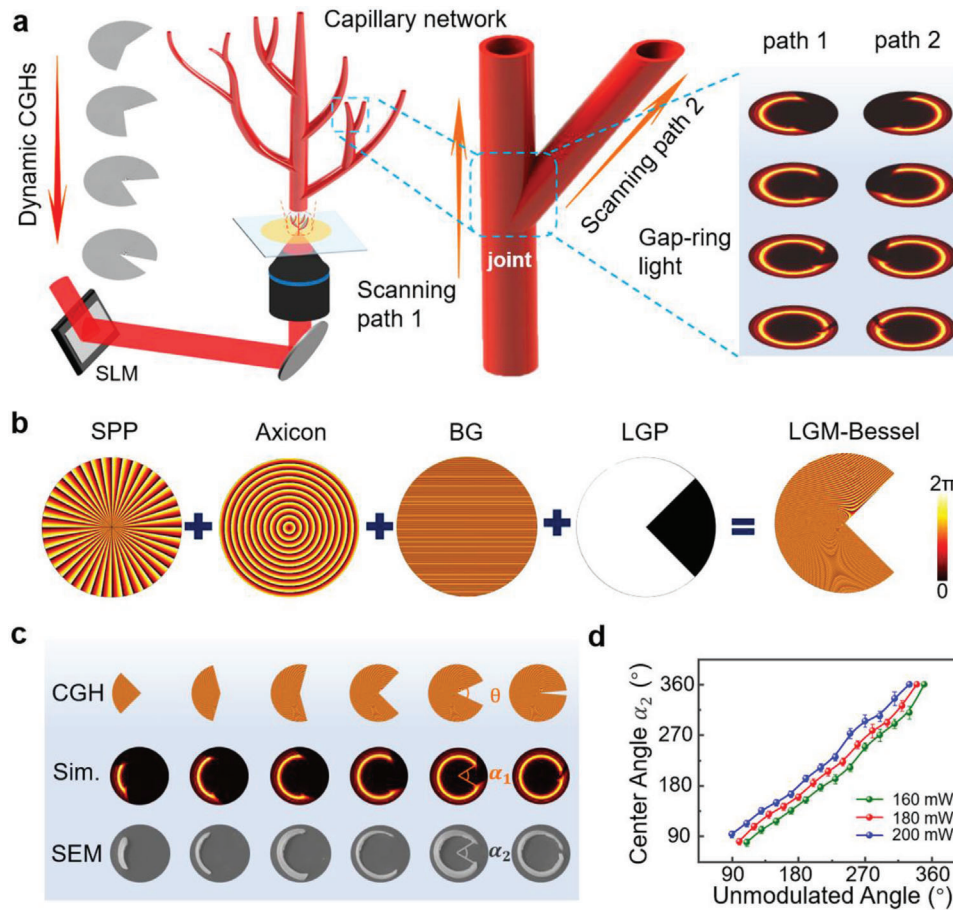


Figure 1. Optimal design and fabrication of bifurcated microtubes with controllable gap shapes. a) The concept diagram of complex biomimetic microtube networks was rapidly prepared by a dynamic holographic processing method. b) The LGM-Bessel CGH for generating gap-ring light is composed of SPP, Axicon, BG and local phase modulation. c) Flexible adjustment of the center angle of the gap-ring. The first line is CGHs with different modulation angles θ and the same $n = 40$ and $r_0 = 400$ (the value of θ from left to right is 270° , 210° , 150° , 90° , 50° , and 10°). The second line and third line correspond to the simulated light intensity distribution and SEM images of gap-ring structures. d) The center angle of the gap-ring structures increases with increasing unmodulated angle. Different line colors represent different laser powers.

Taking the measurement error into account, the change in α_2 can be regarded as 45° linear with the change in unmodulated angle, which indicates that α_2 can be precisely controlled by adjusting θ . Therefore, a gap-ring Bessel beam with controllable energy distribution can be generated by superimposing an LGP onto the holograms, which lays a foundation for the precise processing of bifurcated microtubes.

2.2. Rapid Processing of Bifurcated Microtubes with Complex Morphologies

Capillaries extend forward in an indefinite number of branches and diverse morphologies in vivo. To simulate the branching morphologies of a real blood capillary, bifurcated microtubes with different branch numbers are fabricated by the dynamic holographic method. When two cylinders intersect, a spatial curve is formed at their common surface, which is called the intersecting line in space geometry. Here, the natural curve was utilized to design the joint of bifurcated microtubes. By syner-

gistically controlling the dynamic loading of the holograms and the movement of the translation stage, bifurcated microtubes can achieve precise and smooth splicing (Figure 1a). The yellow curve in Figure 2a is the intersecting line generated automatically by software, and a series of varied blue and orange gap-rings converge to the intersecting line at different cross sections of the joint. To illustrate the splicing process, two sections of the joint of bifurcated microtubes are extracted (the left of Figure 2a). During processing from section 1 to section 2:

$$\Delta\beta = \beta_2 - \beta_1 \quad (3)$$

$$\Delta x = x_2 - x_1 = R(\sin\beta_2 - \sin\beta_1) \quad (4)$$

where $\Delta\beta$ is the half change in the center angle α_1 of the gap-ring beam, R is the radius of the microtube and Δx is the increment of the gap-ring beam in the x direction. Since gap-ring

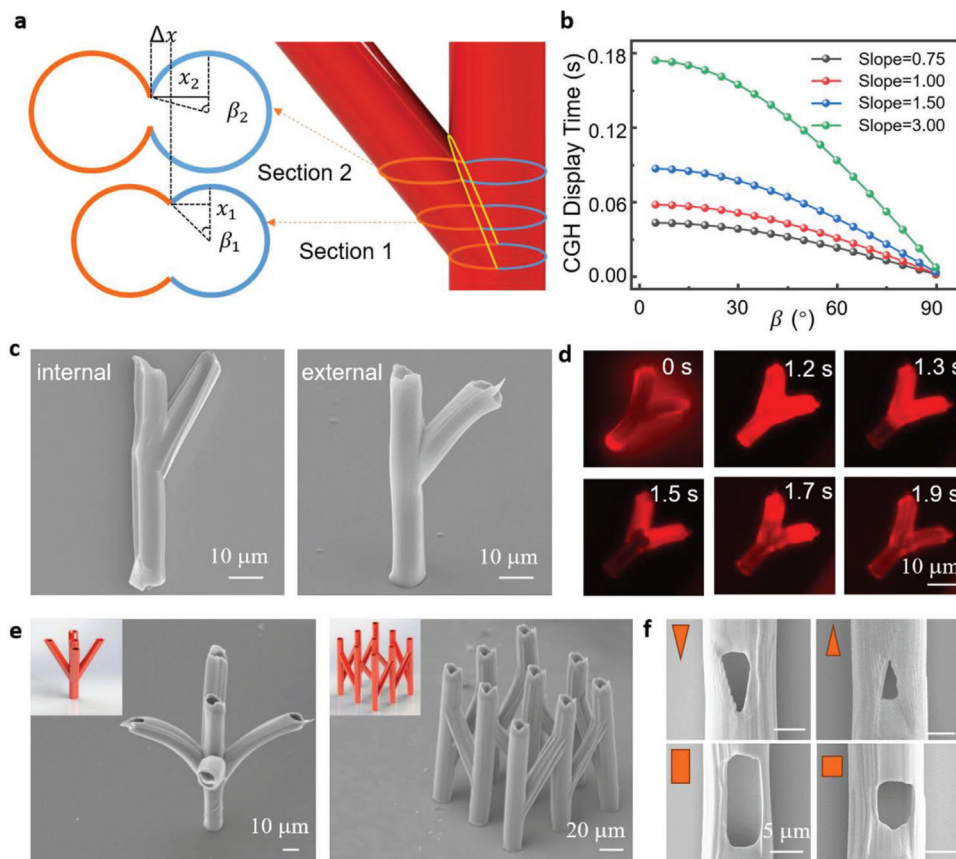


Figure 2. Optimal design and fabrication of bifurcated microtubes with controllable gap shapes. a) Schematic diagram of the processing joint of bifurcated microtubes by the splicing method of dynamic gap-ring lights. b) The hologram displays that the time of LPM-Bessel CGH gradually decreases with increasing β . Different line colors represent different slopes of branching. c) External and internal views of a single branch microtube with a 12 μm diameter and 30° bifurcation angle. d) Fluorescence images of rhodamine solution conducting in a Y-shaped microtube in a very short time. e) SEM images of simple bifurcated microtubes and complex biomimetic microtube networks. f) Dynamic holography rapidly processes gaps of different shapes (square, rectangle, triangle) on a microtube. Scale bars, (f) 5 μm .

beam changes under scans are symmetric to each other, the following relationship can be obtained:

$$\Delta\beta \rightarrow 2\Delta x \quad (5)$$

When the α_1 angle changes $2\Delta\beta$, diagonal scanning compensates for the moving distance of $2\Delta x$ in the x direction. Based on this principle, bifurcated microtube branching at any angle can be fabricated with optimal fluidity and permeability of the solution.

Combining the above inferences, the display time of CGHs can be described as:

$$\Delta t = \frac{\Delta X}{v_x} = \frac{2\Delta x}{v_x} = \frac{2R(\sin\beta_2 - \sin\beta_1)}{v_x} \quad (6)$$

where ΔX is the displacement of the platform in the x direction, and $\Delta X = 2\Delta x$ is set to compensate for the gap-ring beam change. v_x is the scanning speed in the x direction which is set as a constant in the joint to simplify the design of the dynamic CGH display time. The display times of CGHs for processing bifurcated microtubes with different slopes are shown in Figure 2b. In

fact, the calculated display frequencies of CGHs are higher than the refresh frequencies of an SLM in the last few frames, which would induce a gap on a joint of bifurcated microtubes in theory. However, the LGPM method does not modulate the gap-ring beam smoothly. Under high processing power (>130 mW), the orbital Hall effect,^[41] is apparent at the gaps of structures when the modulation angle θ is lower than 110°, which leads to a reduction in the actual gap size of gap-ring structures (Figure S4, Supporting Information). When the modulation angle θ is lower than 40°, the gap disappears. This optical property is beneficial to the fabrication of bifurcated microtubes as redundant structures to compensate for the gaps caused by the insufficient refresh frequency of the SLM.

Figure 2c shows the SEM images of the internal and external regions of a single branching microtube, in which the external connection of bifurcated microtubes is in good condition without cracks and the internal connection is smooth with no redundant structure blocking the microtubes. It is worth mentioning that the observation of the internal structure does not require cumbersome plasma cutting, and only utilizes the local grayscale phase modulation method to adjust half of the CGH phase to zero (Movie S1, Supporting Information), which is also applicable to

any cutting of the holographic light field. To verify the fluid fluidity of bifurcated microtubes, 1 μL of rhodamine solution was dropped on the Y-shaped microtube and then most of the liquid was immediately removed with a pipette. As the liquid evaporated, the residual liquid was instantly sucked into the microtube by capillary force, and it was observed that the microtube was instantly filled with red fluorescence. Subsequently, the solution evaporated in the microtube and the red fluorescence gradually disappeared within 2 s, demonstrating the good liquid fluidity of the Y-shaped microtube (Figure 2d). The fluidity tests of other bifurcated microtubes with different branch numbers are provided in Movies S2–S5 (Supporting Information). The SEM images and modeling diagrams of processed bifurcated microtubes with different branch numbers are shown in Figure 2e; Figure S5 (Supporting Information). It is worth noting that all branches extend from the same position of the main microtubes.

Based on the above design of bifurcated microtubes, biomimetic 3D microtube networks with complex shapes are rapidly manufactured, which exhibits the flexibility of our processing method (Figure 2e and Figure S6, Supporting Information). The dynamic light field for fabricating arborization microtube networks is provided in Movie S6, Supporting Information. In addition, by flexibly designing the permutation and display time of CGHs, gaps of different shapes, such as square, triangle, and rectangle, can be obtained on microtube walls, which further demonstrates the universality of our processing method (Figures 2f). The processing time of these biomimetic microtubes is only several seconds to tens of seconds when using scanning speeds of $30 \mu\text{m s}^{-1}$. Compared to the single point scanning strategy, the processing efficiency can be improved at least 30 times.^[42] Such a high-speed processing method makes it possible to quickly manufacture microtube networks with designable morphologies on a large scale. In addition, this fan-shaped mask method allows for easy and precise control over the center angle, enabling the real-time generation of different gap-ring light fields with varying diameters. Moreover, regardless of the adjusted angle and diameter, the gap-ring light field maintains strict concentric characteristics, ensuring a stable distance from the center. This stability can enhance the accuracy of rapid processing of complex microtube networks. Although there are certain limitations in processing materials and the overall size of the structures currently, these limitations can be overcome by using biocompatible photopolymerizable materials and upgrading the hardware conditions of the manufacturing system. By doing so, more complex and functional microvascular networks can be fabricated, thereby enhancing their applications in the field of biomedicine.

2.3. Generation of Multi-gap Ring Beam for Rapidly Processing Biomimetic Porous Microtubes

Creating biomimetic micropores on the wall of microtube is beneficial for promoting the exchange of substances inside and outside the microtube. Here, the LGPM method is more flexibly utilized to selectively modulate multiple sector areas of the Bessel CHG. As shown in Figure 3a, multigap ring light (MGRL) is generated by modulating 8 centrally symmetrical sector areas of the Bessel beam, and multigap ring structures are obtained

while moving the sample stages by loading the MGRL CGH. It can be seen from the SEM images that the shape of multi-gap annular structures is highly consistent with the MGRL. By adopting the local grayscale phase modulation method, multi-gap ring structures with controllable parameters (gap number, size and position) can be flexibly fabricated (Figure 3a), which greatly promotes the flexibility of MGRL processing microstructures. Notably, due to the unique light intensity distribution of MGRL, it can be used to fabricate 3D cell scaffolds for cell culture. Based on the dynamic holographic processing method, biomimetic porous microtubes can be fabricated with a high processing speed (Figure 3b; Movie S7, Supporting Information). The width of the pore perpendicular to the axis of the microtube is defined as the pore size. Theoretically, microtubes with uniform pore sizes can be obtained with the same modulation parameters. Nevertheless, due to the influence of laser quality and position accuracy of optical components, the intensity distribution of ring light is not uniform, which will result in some differences in the actual pore size of porous microtubes. In addition, the pore size and the number of pore sizes can be tuned by adjusting the process parameters, and the substance exchange between the inside and outside of the porous microtubes can be controlled. As shown in Figure 3c, larger pores can be obtained by increasing the modulation angle θ , and increasing the laser power will reduce the pore size and produce a rougher surface of the microtubes. Similarly, the number of pores can be controlled by altering the number of modulation areas. By adjusting the parameters θ and laser power, the pore size can be flexibly controlled in the range of $0.5 \approx 3.7 \mu\text{m}$ (Figure 3d). Although this method has a high processing speed for producing porous microtubes, there are still some limitations. As TPP is a nonlinear process, when the laser power is too large and the modulated θ is too small, the pores cannot be fabricated due to the intense polymerization reaction of the photoresist. When, the laser power is too small and the modulated θ is too large, the porous microtubes will collapse due to insufficient strength. Therefore, 190 mW laser power and 22° modulation angle θ are selected to ensure sufficient mechanical strength and proper pore size (average $2 \mu\text{m}$) for subsequent experiments.

2.4. Vascularization of 3D Real-Scale Morphology-Programmable Biological Hybrid Capillary Networks

Capillaries are the thinnest blood vessels with a simple physiological structure,^[43] and the vascular wall is composed of only a flat layer of endothelial cells. Herein, human umbilical vein endothelial cells (HUVECs) are cultured with porous microtubes to develop 3D biohybrid capillaries.^[44] Single-layer HUVECs covering biomimetic porous microtube scaffolds represent a simple and effective capillary that can be used in biomedicine studies, such as hormone delivery and drug transport across membranes.

The concept diagram of the biohybrid capillary is shown in Figure 4a. HUVECs develop around porous microtube scaffolds to form a 3D capillary. Vascular endothelial cadherin (VE-cadherin) is a primary component of adherens junctions between endothelial cells and a key molecule that regulates vascular permeability. In this study, we used immunofluorescence

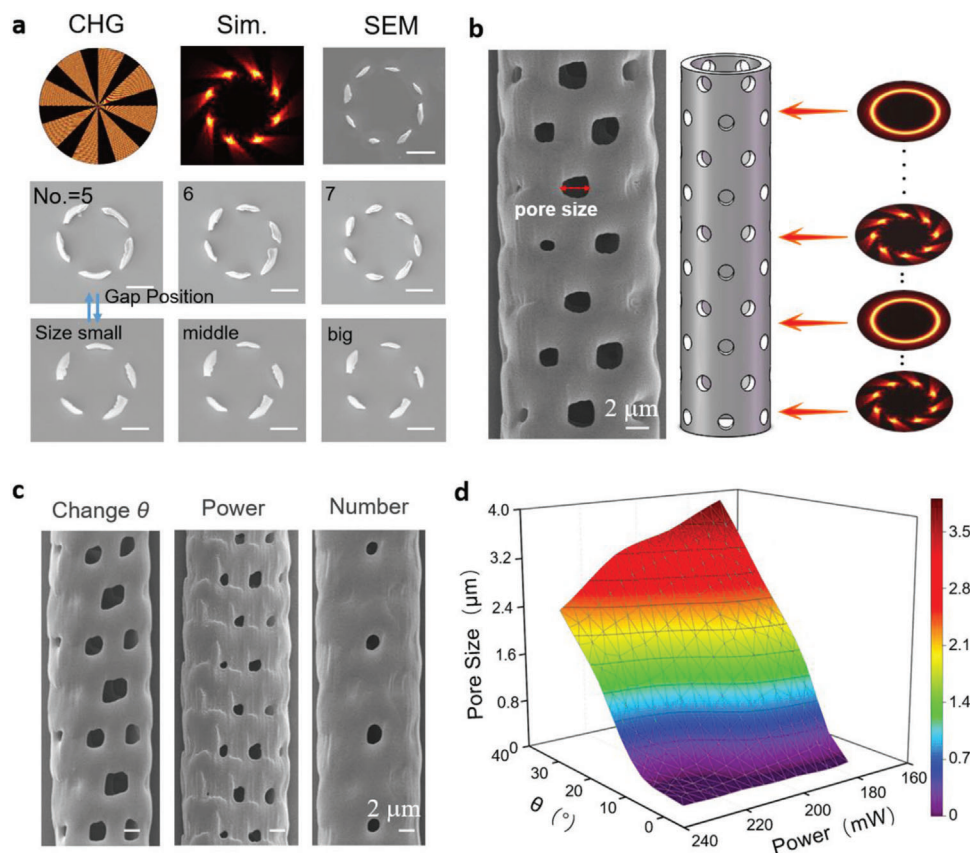


Figure 3. Generation of multi-gap ring light for rapidly processing biomimetic porous microtubes. a) Multiarea local phase modulated Bessel CGH ($n = 40$, $r_0 = 400$, $\theta = 18^\circ$ and modulation area number 8 is shown in the left panel of the first line for generating MGRL (middle) to produce multi-gap ring structures (right). The gap number, size and position could be flexibly controlled, as shown in the second and third lines. b) The processing method of biomimetic porous microtubes (right) and SEM images of porous microtubes with a diameter of $12 \mu\text{m}$ and a pore size of $2 \mu\text{m}$ (left). c) The size and number of pores can be adjusted by changing the modulation angle θ , laser power and modulation area number. d) The pore diameter is $0.5 \approx 3.7 \mu\text{m}$. Scale bars, a) $5 \mu\text{m}$.

experiments to label vascular endothelial cell adhesion protein with VE-cadherin and cell nuclei with DAPI. The results revealed the formation of preliminary biomimetic capillaries (Figure S7, Supporting Information). The nutrients inside and outside the hybrid capillaries could be transported across the membrane through pores on the wall of the microtubes. To quantitatively study the formation process of capillaries, HUVECs were seeded on porous microtube arrays to observe the growth phenomenon of endothelial cells in different periods. The SEM images of bio-hybrid capillaries on different culture days *in vitro* (1, 2, 3, and 4 days) are shown in Figure 4b, in which endothelial cells are dehydrated and supercritical dried to maintain their original morphology. After 1 day, the coverage ratio of endothelial cells in porous microtube array scaffolds was 19.58%, the majority of endothelial cell bodies were still large, and only a few cells spread out (Figure S8, Supporting Information). After 2 days, the coverage ratio reached 36.89%, endothelial cells proliferated on microtubes and the number of cells increased. A capillary with an open vascular lumen was formed at 3 days (Figure 4b,c,d), and the cell coverage ratio reached 97.49%. Next, we conducted experiments with biomimetic microvessels, featuring varying pore sizes and numbers, to assess their ability to support cell coverage. After 3 days of cultivation, no significant differences in cell coverage

were observed among the different configurations. One potential reason for this outcome is the relatively small overall size of the microtubes. As a result, cells effectively covered the entire surface of the microtubes during the *in vitro* cultivation, making it challenging to discern the impact of pore size and number on the coverage ratio. Additionally, it is worth considering that porous microtubes with diverse pore sizes and numbers might be more suitable for investigating signal transmission and communication between different types of cells.^[45] Endothelial cells tightly and orderly cover the pores of microtube scaffolds, guaranteeing that the cell membrane is a medium for substance exchange. Previous studies have found that thin vascular sprouts can bud from thick blood vessels. However, these sprouts are chaotic and solid, without open vascular lumens, which are not conducive to the exchange of substances inside and outside of blood vessels. In addition, a longer culture time (4 days) led to thicker and denser vascularization (Figure 4b), which means that changing the culture time can control the thickness of the blood vessel wall. The 3D coverage around the microtube scaffolds of endothelial cells is shown in Figure S9 (Supporting Information), and the vascularization quality is good. In addition, live/dead staining experiment was performed to test the cell viability on the scaffold. The absence of significant cell death after the 2 days cultivation

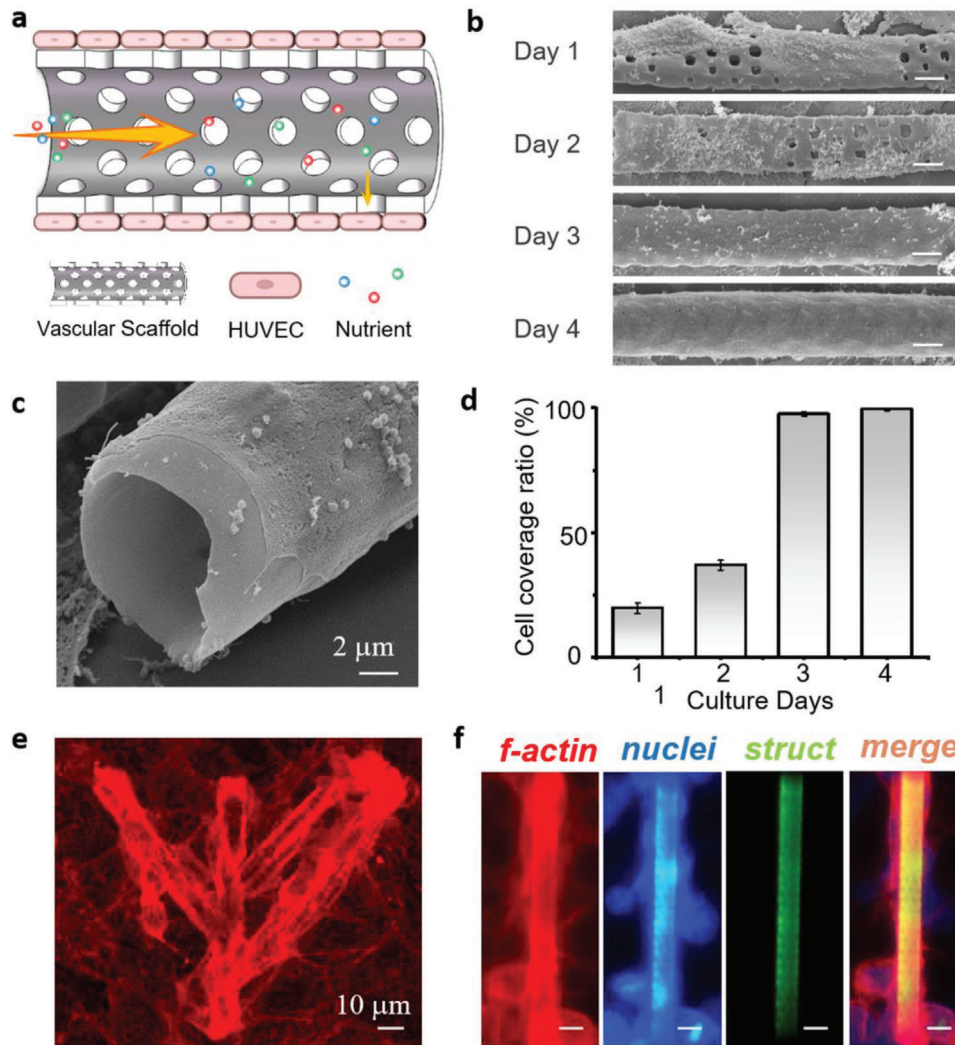


Figure 4. Vasculization of 3D real-scale morphology-programmable biological hybrid capillary networks. a) Concept diagram of nutrient flow in a biohybrid capillary and transmembrane transport through micropores. b) SEM images of the vascularization of HUVECs outside the porous microtubes on different days (1-4 DIV). c) A capillary with an open vascular lumen is formed in 3 days. d) Quantitative evaluation of the coverage ratio of HUVECs on porous microtubes at different culture times. After 3 days, the value reached 97.49%. e) Immunofluorescence images of endothelial cells (F-actin, red, Nuclei, blue) guided by microtube scaffolds to form arborization capillaries. f) Multiple cells adhere around a single microtube, and F-actin has high red fluorescence expression (red) and forms a membrane covering the porous microtubes (green). The culture time for e) and f) is DIV3. Scale bars, (b) 5 μm , (f) 10 μm .

period suggests that the cell culture conditions and medium used in the experiment are supportive of cell viability and proliferation (Figure S10, Supporting Information). Employing data analysis and quantitative assessment on the lower image, it was determined that $\approx 0.4\%$ of cells are non-viable, with $\approx 99.6\%$ maintaining their viability.

To demonstrate the position and tight junctions of endothelial cells, F-actin (red, phalloidine) and nucleus (blue, DAPI) of endothelial cells were stained with immunofluorescence (Figure S11, Supporting Information). Multiple cells (blue) adhered around a single microtube, and F-actin had high red fluorescence expression forming a membrane covering the porous microtubes (green) (Figure 4f). In addition, microtube networks mimicking arborization capillaries are the most common in the

human body and are utilized to guide the vascularization of endothelial cells. High red fluorescence expression of filamentous actin can be observed around arborization microtube networks (Figure 4e), showing that the guidance of endothelial cells by microtube scaffolds for specific morphology vascularization is an effective method. The preparation of biomimetic capillary network scaffolds with this resolution opens up possibilities for simulation and application in various real physiological environments in the future. For example, by accurately simulating the real capillary diameter, researchers can gain better insights into the physiological processes and hemodynamics of microcirculation. Furthermore, these biomimetic capillaries can also be used to simulate the vascular supply network of tumors, leading to a deeper understanding of tumor growth and diffusion mechanisms,

and providing a platform for the development of anti-tumor drugs.

3. Conclusion

In summary, an efficient femtosecond dynamic holographic processing method is proposed to rapidly produce biomimetic microtube networks with complex morphologies. Bifurcated microtubes with smooth connections and good liquidity are prepared by utilizing a series gap-ring light with precise controllable center angles. Compared with the conventional point-by-point scanning strategy, the processing speed is increased by at least 30 times. Moreover, to facilitate substance exchange, biomimetic porous microtubes with adjustable parameters are flexibly manufactured by introducing the dynamic processing of the MGRL. Finally, biomimetic porous microtube networks were used as scaffolds to culture endothelial cells. After 3 days, HUVECs around the porous scaffolds formed tight junctions and 3D coverage, which indicated that the scaffolds played a significant role in the densification of blood vessels. Currently, organ chips have become essential biomedical engineering tools that enable the construction and simulation of human organ structures and functions on a chip. Building transport circulation systems based on vascular networks is crucial for the development of organ chips, and the fabrication of capillary networks has been a challenging task. Our work provides a novel, flexible and rapid method for the construction of microvascular networks in microfluidic chips. In the future, by combining dynamic holographic processing with other micro/nano technologies and bioengineering methods, more sophisticated and physiologically relevant organ chips can be fabricated, which will further enhance the capabilities and applications of organ chips.

4. Experimental Section

Fabrication of Microtube Networks: A typical holographic femtosecond laser direct writing system was used for rapid fabrication of microtube networks. The light source was a mode-locked Ti:sapphire laser oscillator (Chameleon Vision-S, Coherent Corp, central wavelength: 800 nm, repetition rate: 80 MHz, pulse width: 75 fs), and the femtosecond Gaussian beam was modulated by a reflective liquid crystal SLM (Pluto NIR II, Holoeye) with 1920×1080 pixels, the pixel pitch of 8 μm , and 256 gray levels. Designed LPM-Bessel CGHs were dynamically loaded on SLM to produce a series of gap-ring light fields, which were focused by a 60x oil immersion lens (Olympus) with high NA (1.35) to improve processing quality. A commercially available zirconium-silicon hybrid sol-gel material doped with 4,4'-bis(diethylamino)-benzophenone photoinitiator at 1% by weight (SZ2080, IESLFORTH) was used for photopolymerization, which was negligibly shrinkable compared with other photoresists. The sample was pre-baked to evaporate the solvent on a 100 °C platform for 40 min. The precise displacement motion of the sample was realized by nanopositioning stage (E545, Physik Instrument) with a nanometer resolution and a $200 \times 200 \times 200 \mu\text{m}$ moving range. The displacement control program was compiled in Visual Studio 2013 by c++ language to achieve complex curvilinear motion. After polymerization, the sample was developed in 1-propanol for 2 h until all unpolymerized parts were washed away. Then the sample was removed from the developer, and microtube networks were obtained on the glass substrate waiting for sterilization and cell seeding.

Vascularization of Cells: Human umbilical vein endothelial cells (HUVECs) were cultured in minimum essential medium (Invitrogen, 11090081) supplemented with 10% fetal bovine serum (FBS, Gibco),

100 U mL^{-1} penicillin, and 100 $\mu\text{g mL}^{-1}$ streptomycin in a humid atmosphere of 5% CO_2 at 37 °C. The sample was hydrophilically treated with a plasma cleaner for 1 minute and washed with alcohol before cell seeding. After 30 min of UV sterilization in the safety cabinet, the dissociated cells were seeded on microtube scaffolds on $\Phi 18$ mm coverslips (Assistant) in 35 mm petri dishes at a density of 30000–50000 cells mL^{-1} and maintained in incubators at 37 °C in 5% CO_2 . Culture medium (1.5 ml) was added to each dish. Then, the petri dishes were transferred to an incubator at 37 °C under a humid atmosphere with 5% CO_2 for cell proliferation and vascularization.

Biological Testing: For immunofluorescence staining, the cells were fixed for 15 min with cold 4% paraformaldehyde in PBS (0.01 mol L^{-1} phosphate buffer solution, pH = 7.4) in an imaging chamber, washed with PBS and permeabilized with Triton X-100 (0.2% Triton X-100 in PBS). Fixed and permeabilized neurons were blocked in 3% BSA in PBS for 1 h, F-actin was stained with phalloidine for 1 h, and nucleus were stained with DAPI for 15 min. After each staining, the sample was washed twice with PBS. Stained cells were visualized under a fluorescence microscope (Leica DMI3000B).

SEM images of endothelial cells were derived from samples cultured in vitro for 3 days. These samples were washed with DPBS and then fixed with 4% paraformaldehyde (PFA) in DPBS at 4 °C for 20 min. Progressive and gradual dehydration steps were carried out by rinsing the samples with increasing ethanol solutions (0%, 5%, 10%, 20%, 30%, 50%, 70%, 90%, 95%, and 100% in deionized water). The samples were then dried under supercritical conditions and sputtered with gold before scanning electron microscope investigation. The growth of cells in microtube networks was observed more clearly by scanning electron microscopy (FEI Sirion200).

Quantitative Analysis of Vascularization: Quantitative analysis was realized by manually outlining the outer contour of each identifiable endothelial cell using Fiji/ImageJ software.

Supporting Information

Supporting Information is available from the Wiley Online Library or from the author.

Acknowledgements

B.W.S., C.W.W., and S.Y.F. contributed equally to this article. This work was supported by the National Key Research and Development Program of China (No. 2021YFF0502700), the National Natural Science Foundation of China (Nos. 51675503, 52075516, 62005262, 61927814, 62105319, 62105090), CAS Project for Young Scientists in Basic Research (No. YSBR-049), the Major Scientific and Technological Projects in Anhui Province (No. 202103a05020005), the USTC Research Funds of the Double First-Class Initiative (YD2340002009) and the Open Project of Wuhan National Laboratory for Optoelectronics (No. 2019WNLOKF014). The authors acknowledge the Experimental Center of Engineering and Material Sciences at USTC for the fabrication and measuring of samples. This work was partly carried out at the USTC Center for Micro and Nanoscale Research and Fabrication.

Conflict of Interest

The authors declare no conflict of interest.

Data Availability Statement

The data that support the findings of this study are available in the supplementary material of this article.

Keywords

biomimetic bifurcated microtube scaffolds, biomimetic porous microtubes, capillary networks, dynamic holographic processing, two-photon polymerization

Received: May 11, 2023

Revised: August 18, 2023

Published online:

- [1] S. Murphy, A. Atala, *Nat. Biotechnol.* **2014**, *32*, 773.
- [2] S. You, Y. Xiang, H. Hwang, D. Berry, W. Kiratitanaporn, J. Guan, E. Yao, M. Tang, Z. Zhong, X. Ma, D. Wangpraseurt, Y. Sun, T. Lu, S. Chen, *Sci. Adv.* **2023**, *9*, eade7923.
- [3] R. Zhang, L. Deng, J. Guo, H. Yang, L. Zhang, X. Cao, A. Yu, B. Duan, *ACS Nano* **2021**, *15*, 17790.
- [4] J. Brassard, M. Nikolaev, T. Hubscher, M. Hofer, M. Lutolf, *Nat. Mater.* **2021**, *20*, 22.
- [5] L. Niklason, J. Lawson, *Science* **2020**, *370*, eaaw8682.
- [6] C. O'Connor, E. Brady, Y. Zheng, E. Moore, K. Stevens, *Nat. Rev. Mater.* **2022**, *7*, 702.
- [7] J. Yu, J. Navarro, J. Coburn, B. Mahadik, J. Molnar, J. Holmes, A. Nam, J. Fisher, *Adv. Healthcare Mater.* **2019**, *8*, 1801471.
- [8] H. Thorp, K. Kim, M. Kondo, T. Maak, D. Grainger, T. Okano, *Cells* **2021**, *10*, 643.
- [9] S. Yin, W. Zhang, Z. Zhang, X. Jiang, *Adv. Healthcare Mater.* **2019**, *8*, 1801433.
- [10] E. Fioretta, S. Motta, V. Lintas, S. Loerakker, K. Parker, F. Baaijens, V. Falk, S. Hoerstrup, M. Emmert, *Nat Rev Cardiol* **2021**, *18*, 92.
- [11] N. Noor, A. Shapira, R. Edri, I. Gal, L. Wertheim, T. Dvir, *Adv. Sci.* **2019**, *6*, 1900344.
- [12] Q. Jallerat, A. W. Feinberg, *Cells* **2020**, *9*, 285.
- [13] J. Wang, H. Ren, Y. Liu, L. Sun, Z. Zhang, Y. Zhao, X. Shi, *Adv. Healthcare Mater.* **2021**, *10*, 2101580.
- [14] N. S. Bhise, V. Manoharan, S. Massa, A. Tamayol, M. Ghaderi, M. Miscuglio, Q. Lang, Y. Shrike Zhang, S. R. Shin, G. Calzone, N. Annabi, T. D. Shupe, C. E. Bishop, A. Atala, M. R. Dokmeci, A. Khademhosseini, *Biofabrication* **2016**, *8*, 014101.
- [15] A. Moya, M. Ortega-Ribera, X. Guimera, E. Sowade, M. Zea, X. Illa, E. Ramon, R. Villa, J. Gracia-Sancho, G. Gabriel, *Lab Chip* **2018**, *18*, 2023.
- [16] J. Potkay, *Lab Chip* **2014**, *14*, 4122.
- [17] Y. Zhu, L. Sun, Y. Wang, L. Cai, Z. Zhang, Y. Shang, Y. Zhao, *Adv. Mater.* **2022**, *34*, 2108972.
- [18] K. M. Kovach, M. A. LaBarbera, M. C. Moyer, B. L. Cmolik, E. van Lunteren, A. S. Gupta, J. R. Capadona, J. A. Potkay, *Lab Chip* **2015**, *15*, 1366.
- [19] G. Yang, B. Makadik, J. Choi, J. Fisher, *Prog. Biomed. Eng.* **2020**, *2*, 012002.
- [20] A. Enrico, D. Voulgaris, R. Ostmans, N. Sundaravadeivel, L. Moutaux, A. Cordier, F. Niklaus, A. Herland, G. Stemme, *Adv. Mater.* **2022**, *34*, 2109823.
- [21] C. Bettinger, E. Weinberg, K. Kulig, J. Vacanti, Y. Wang, J. Borenstein, R. Langer, *Adv. Mater.* **2006**, *18*, 165.
- [22] Y. Zheng, J. Chen, M. Craven, N. Choi, S. Totorica, A. Diaz-Santana, P. Kermani, B. Hempstead, C. Fischbach-Teschl, J. Lopez, A. Stroock, *Proc. Natl. Acad. Sci. USA* **2012**, *109*, 9342.
- [23] R. W. Barrs, J. Jia, S. E. Silver, M. Yost, Y. Mei, *Chem. Rev.* **2020**, *120*, 10887.
- [24] S. Singh, B. Wu, J. Dunn, *Biomaterials* **2011**, *32*, 2059.
- [25] X. Zhao, L. Liu, J. Wang, Y. Xu, W. Zhang, G. Khang, X. Wang, *J. Tissue Eng. Regener. Med.* **2016**, *10*, 833.
- [26] J. Temple, D. Hutton, B. Hung, P. Huri, C. Cook, R. Kondragunta, X. Jia, W. Grayson, *J. Biomed. Mater. Res., Part A* **2014**, *102*, 4317.
- [27] J. Miller, K. Stevens, M. Yang, B. Baker, D. Nguyen, D. Cohen, E. Toro, A. Chen, P. Galie, X. Yu, R. Chaturvedi, S. Bhatia, C. Chen, *Nat. Mater.* **2012**, *11*, 768.
- [28] D. Kolesky, R. Truby, A. Gladman, T. Busbee, K. Homan, J. Lewis, *Adv. Mater.* **2014**, *26*, 3124.
- [29] L. Yang, F. Mayer, U. H. F. Bunz, E. Blasco, M. Wegener, *Light Adv. Manuf.* **2021**, *2*, 17.
- [30] H. Yu, H. Ding, Q. Zhang, Z. Gu, M. Gu, *Light Adv. Manuf.* **2021**, *2*, 31.
- [31] S. Zhang, S. Li, X. Wan, J. Ma, N. Li, J. Li, Q. Yin, *Addit. Manuf.* **2021**, *47*, 102358.
- [32] J. Song, C. Michas, C. S. Chen, A. E. White, M. W. Grinstaff, *Adv. Healthcare Mater.* **2020**, *9*, 1901217.
- [33] A. Marino, O. Tricinci, M. Battaglini, C. Filippeschi, V. Mattoli, E. Sinibaldi, G. Ciofani, *Small* **2018**, *14*, 1702959.
- [34] A. Dobos, F. Gantner, M. Markovic, J. Hoorick, L. Tytgat, S. Vlierberghe, A. Ovsianikov, *Biofabrication* **2020**, *13*, 015016.
- [35] A. Balena, M. Bianco, F. Pisanello, M. Vittorio, *Adv. Funct. Mater.* **2023**, 2211773.
- [36] D. Yang, L. Liu, Q. Gong, Y. Li, *Macromol. Rapid Commun.* **2019**, *40*, 1900041.
- [37] P. Somers, Z. Liang, J. Johnson, B. Boudouris, L. Pan, X. Xu, *Light: Sci. Appl.* **2021**, *10*, 199.
- [38] P. Salter, M. Booth, *Light: Sci. Appl.* **2019**, *8*, 110.
- [39] S. Ji, L. Yang, Y. Hu, J. Ni, W. Du, J. Li, G. Zhao, D. Wu, J. Chu, *Small* **2017**, *13*, 1701190.
- [40] L. Yang, D. Qian, C. Xin, Z. Hu, S. Ji, D. Wu, Y. Hu, J. Li, W. Huang, J. Chu, *Opt. Lett.* **2017**, *42*, 743.
- [41] C. Cisowski, R. Correia, *Opt. Lett.* **2018**, *43*, 499.
- [42] C. Xin, L. Yang, J. Li, Y. Hu, D. Qian, S. Fan, K. Hu, Z. Cai, H. Wu, D. Wang, D. Wu, J. Chu, *Adv. Mater.* **2019**, *31*, 1808226.
- [43] S. Fleischer, D. N. Tavakol, G. Vunjak-Novakovic, *Adv. Funct. Mater.* **2020**, *30*, 1910811.
- [44] D. J. Medina-Leyte, M. Domínguez-Pérez, I. Mercado, M. T. Villarreal-Molina, L. Jacobo-Albavera, *Appl. Sci.* **2020**, *10*, 938.
- [45] R. Arayanarakool, A. K. Meyer, L. Helbig, S. Sanchez, O. G. Schmidt, *Lab Chip* **2015**, *15*, 2981.